Monthly Notices of the ROYAL ASTRONOMICAL SOCIETY

MNRAS **526,** 1687–1698 (2023) https://doi.org/10.1093/mnras/stad2775
Advance Access publication 2023 September 18

BASS-XL: X-ray variability properties of unobscured active galactic nuclei

Alessia Tortosa [1,2★] Claudio Ricci [1,3,4] Patricia Arévalo [5] Michael J. Koss [6] Franz E. Bauer,[7,8,9,10] Benny Trakhtenbrot [11] Richard Mushotzky,[12,13] Matthew J. Temple [1] Federica Ricci,[2,14] Alejandra Rojas Lilayu [1,15] Taiki Kawamuro,[16] Turgay Caglar,[17] Tingting Liu,[18] Fiona Harrison,[19] Kyuseok Oh,[20,21] Meredith Clark Powell,[22] Daniel Stern[23] and Claudia Megan Urry[24]

Affiliations are listed at the end of the paper

Accepted 2023 September 5. Received 2023 August 3; in original form 2023 June 1

ABSTRACT

We investigate the X-ray variability properties of Seyfert 1 Galaxies belonging to the BAT AGN Spectroscopic Survey (BASS). The sample includes 151 unobscured ($N_{\rm H} < 10^{22}$ cm^{-2}) AGNs observed with *XMM–Newton* for a total exposure time of ∼27 ms, representing the deepest variability study done so far with high signal-to-noise *XMM–Newton* observations, almost doubling the number of observations analysed in previous works. We constrain the relation between the normalized excess variance and the 2–10 keV AGN luminosities, black hole masses, and Eddington ratios. We find a highly significant correlation between $\sigma^2_{\rm NXS}$ and $M_{\rm BH}$, with a scatter of ∼0.85 dex. For sources with high L_{2-10} this correlation has a lower normalization, confirming that more luminous (higher mass) AGNs show less variability. We explored the $\sigma^2_{\rm NXS}$ versus $M_{\rm BH}$ relation for the sub-sample of sources with $M_{\rm BH}$ estimated via the 'reverberation mapping' technique, finding a tighter anticorrelation, with a scatter of ∼0.65 dex. We examine how the $\sigma^2_{\rm NXS}$ changes with energy by studying the relation between the variability in the hard (3–10 keV) and the soft (0.2–1 keV)/medium (1–3 keV) energy bands, finding that the spectral components dominating the hard energy band are more variable than the spectral components dominating in softer energy bands, on time-scales shorter than 10 ks.

Key words: quasars: supermassive black hole – X-rays: galaxies – black hole physics – galaxies:nuclei.

1 INTRODUCTION

Supermassive Black Holes (SMBHs; $M_{\rm BH} > 10^6$ M$_\odot$) are ubiquitously found at the centre of massive galaxies. Mass accretion onto SMBHs is the mechanism that powers active galactic nuclei (AGNs; Salpeter 1964) which are very powerful sources of X-ray radiation, emitting through the entire electromagnetic spectrum. Variability is a distinctive feature shared by all classes of AGN, occurring over a wide range of time-scales and amplitudes across all the wavelengths (e.g. Ulrich, Maraschi & Urry 1997; McHardy et al. 2004). These flux variations can also be accompanied by prominent spectroscopic changes (e.g. Ricci & Trakhtenbrot 2022). In the X-ray band, variability is observed on both short (e.g. $<10^3$ s; Uttley & McHardy 2005; McHardy et al. 2004) and long time-scales (e.g. years; McHardy 2001; Ishibashi & Courvoisier 2009; Sartori et al. 2018) giving insight into the innermost regions of the AGN. Thus, its study can help us to understand the emission properties of AGNs (e.g. Mushotzky, Done & Pounds 1993; Ulrich et al. 1997; Uttley et al. 2014; Cackett, Bentz & Kara 2021; De Marco, Motta & Belloni 2022) and better characterize the growing population of extremely variable AGNs identified in the optical (e.g. Lawrence et al. 2016; Rumbaugh et al. 2018; Trakhtenbrot et al. 2019; Shen 2021; Zeltyn et al. 2022; Temple et al. 2023) and X-rays (e.g. Ricci et al. 2020, 2021; Timlin et al. 2020; Masterson et al. 2022).

One method used to study the temporal structure of the variations is the power spectral density (PSD) analysis. If the temporal frequency is $\nu = 1/t$, where t is the time, the observed power spectrum is generally modelled as a power-law of the form: $P_\nu \propto \nu^\alpha$. For short time-scales (high frequencies) $\alpha \sim -2$, while for long time-scales (low frequencies) $\alpha \sim -1$ (Papadakis & McHardy 1995). The PSD break time-scales, $T_{\rm B}$, can be obtained by fitting a broken power laws to the observed PSD. This parameter has been found to be positively correlated with the black hole mass ($M_{\rm BH}$; e.g. Lu & Yu 2001; Bian & Zhao 2002; Uttley, McHardy & Papadakis 2002; Markowitz, Edelson & Vaughan 2003; Papadakis 2004). However, Narrow Line Seyfert 1(NLS1) galaxies, which typically accrete at very high Eddington ratios ($L_{\rm bol}/L_{\rm Edd} = \lambda_{\rm Edd}$; McHardy et al. 2004), display a different behaviour, with their break time-scales being shorter for a given $M_{\rm BH}$. To explain this, Uttley & McHardy (2005) suggested that the break time-scales could depend also on a second parameter, such as the accretion rate or the black hole spin.

Accurately determining the AGNs power spectra can be difficult, since it requires high-quality data, long exposures, and sometimes monitoring campaigns, to extend time coverage that adequately covers relevant PSD frequency ranges that include potential breaks. Given such difficulties, it is common practice to quantify the X-ray variability of AGNs in terms of the so-called normalized excess variance ($\sigma^2_{\rm NXS}$; Nandra et al. 1997). Although it does not contain the same amount of information as the PSD, the normalized excess variance can be used to confirm the PSD results in large samples of AGN, and it also allows the discovery of new correlations between

★ E-mail: alessiatortosa@gmail.com

the X-ray variability amplitude and other AGNs physical parameters. The normalized excess variance of AGNs has been widely studied in the past decades, finding that $\sigma^2_{\rm NXS}$ has a strong dependence on $M_{\rm BH}$. Using the data from the *Advanced Satellite for Cosmology and Astrophysics* (*ASCA*), Lu & Yu (2001) and Bian & Zhao (2003) found an anticorrelation between the excess variance (on a time-scales of ∼1 d) and $M_{\rm BH}$. Papadakis (2004), using *Rossi X-Ray Timing Explorer* data on much longer time-scales (∼300 d), also found an anticorrelation between these two parameters. Ponti et al. (2012) investigated this relation using high quality *XMM–Newton* data on time-scales of 10 ks. They found that the $\sigma^2_{\rm NXS}$–$M_{\rm BH}$ relation flattens for masses below $\sim 10^6$ $M_\odot$, as confirmed later also by Ludlam et al. (2015) studying a sample of low mass AGNs observed by *XMM–Newton*. Akylas, Papadakis & Georgakakis (2022), using light curves of local Seyfert from the Nuclear Spectroscopic Telescope Array hard X-ray mission (*NuSTAR*), extended the $\sigma^2_{\rm NXS}$ versus $M_{\rm BH}$ relation to energy band higher than 10 keV, finding that it is possible to accurately measure the $M_{\rm BH}$ in AGN using the above-mentioned correlation in the 3–10 and the 10–20 keV bands. However, the minimum necessary S/N is ∼3 and duration of the light curves should be ∼80–100 ks.

Several works suggested that the excess variance is related to other source properties, such as the X-ray luminosity, L_{2-10} , (Barr & Mushotzky 1986; Nandra et al. 1997; Turner et al. 1999). However, studying a sample of 46 AGNs observed by *ASCA*, Papadakis (2004) found that once the dependence of $\sigma^2_{\rm NXS}$ from $M_{\rm BH}$ is removed, the correlation between $\sigma^2_{\rm NXS}$ and L_{2-10} is no longer present, implying that the correlation with L_{2-10} was associated to the $\sigma^2_{\rm NXS} - M_{\rm BH}$ relation. The same effect was recovered by O'Neill et al. (2005).

Past studies of hard X-ray selected AGNs with *Swift*/BAT data, focusing on longterm light curves show that in most of these AGNs a significant variability on months to years time-scales is present. In general this variation is not related to changes of the absorption column density but to variations of the power-law continuum (Soldi et al. 2014). Moreover, unlike previous studies, no correlation between hard X-ray variability and different properties of the AGNs including luminosity and black hole mass was found (Shimizu & Mushotzky 2013). Also Phillipson, Vogeley & Boyd (2023), studying the hard X-ray variability properties of *Swift*/BAT AGNs, show that type 1 AGNs in the 14–150 keV band, are found to be less prone to harboring deterministic variability than type 2 AGNs on time-scales of ∼15 yr.

In this paper, we present the results from an excess variance analysis of a sample of 151 hard X-ray selected, unobscured ($N_{\rm H} < 10^{22}$ cm^{-2}) AGNs using ∼500 high signal-to-noise *XMM–Newton* observations, almost double of the number of observations analysed in previous works (e.g. Ponti et al. 2012), for a total of ∼27 ms exposure time.

The paper is organized as follows: Section 2 presents the selected sample and the data reduction of the sources of our sample. Section 3 describes the timing analysis of the data and the extrapolation of the $\sigma^2_{\rm NXS}$ together with the analysis of the correlation between $\sigma^2_{\rm NXS}$ and several physical parameters of the sources. We summarize and conclude the results of our analysis in Section 4. Standard cosmological parameters ($H = 70$ km s^{-1}Mpc^{-1}, $\Omega_\Lambda = 0.73$, and $\Omega_m = 0.27$) are adopted throughout the paper.

2 THE SAMPLE AND DATA REDUCTION

2.1 The BASS sample

Since its launch in 2004, the Burst Alert Telescope (BAT; Barthelmy et al. 2005) on board the *Neil Gehrels Swift observatory* (Gehrels et al. 2004) has been carrying out an all-sky survey in the 14–195 keV band. Our sample consists of all the unobscured ($N_{\rm H} < 10^{22}$ cm^{-2}), radio quiet, type 1 AGNs belonging to the Swift/BAT AGN Spectroscopic Survey (BASS[1]) which have public *XMM–Newton* observations by December 2022.

Being unbiased by obscuration up to Comptont-thick levels ($N_{\rm H} > 10^{24}$ cm^{-2}; Ricci et al. 2015) and not affected by dust obscuration or star formation, BASS provides an important census of AGNs. It gives a full picture of the bright AGNs in the local Universe, providing the largest available spectroscopic sample of *Swift*/BAT ultra-hard X-ray (14–195 keV) detected AGNs (Oh et al. 2018), complementary with *Swift*, *Chandra*, and *XMM–Newton* for X-ray broad-band (0.5–200 keV) spectral measurements (Ricci et al. 2017). It also includes extensive multiwavelength follow-up data, from optical emission (Oh et al. 2022), high spatial resolution near-IR (Lamperti et al. 2017; Koss et al. 2018), mid- and far-IR emission from *WISE*, *IRAS*, *Spitzer*, *Akari*, and *Herschel* (Ichikawa et al. 2017, 2019; Shimizu et al. 2017) and mm/radio emission (Koss et al. 2021; Kawamuro et al. 2022; Ricci et al. 2023), giving insight on the sample over the broadest possible spectral range.

The first BASS data release (DR1; Koss et al. 2017) reported $M_{\rm BH}$ and X-ray properties for all the 838 AGNs from the *Swift*/BAT 70-month catalogue (Ricci et al. 2017), while the second BASS data release (DR2; Koss et al. 2022a) reports more secure and uniformly assessed $M_{\rm BH}$ for 780 unbeamed AGNs from the 70-month catalogue. The masses are estimated from broad Balmer lines and/or 'reverberation mapping' technique (RM) for type 1s and masers, and from dynamics and/or velocity dispersions for type 2s (Koss et al. 2022c; Mejía-Restrepo et al. 2022; Ricci et al. 2022). Moreover, in the DR2, $\lambda_{\rm Edd}$ ($L_{\rm bol}/L_{\rm Edd}$) are computed using the bolometric luminosities calculated from the intrinsic 14–150 keV luminosities as shown in Ricci et al. (2017) with a bolometric correction of 8 (Koss et al. 2022a). In this work, we considered L_{2-10} , $\lambda_{\rm Edd}$, and $M_{\rm BH}$ values from BASS DR2 (Koss et al. 2022b).

2.2 Data reduction

The X-ray Multi-Mirror Mission (*XMM–Newton*, Jansen et al. 2001) high statistics, low background and uninterrupted light-curves obtained for the sources in this sample are crucial to compute the $\sigma^2_{\rm NXS}$ in large samples of AGN.

The sample of BASS unobscured AGNs is composed by 365 sources, with a median redshift of $z_{\rm med} = 0.035$ (lower than the parent sample median redshift). Of these, 153 had public *XMM–Newton* observations as of December 2022. We downloaded all the observations from the *XMM–Newton* Science Archive, and extracted the EPIC-pn (Strüder et al. 2001) light curves using the Science Analysis System (SAS) software package (v.18.0.0) (Gabriel et al. 2004) and the calibration data base CALDB 20221102. The MOS detectors (Turner et al. 2001) and the Reflection Grating Spectrometer (RGS; den Herder et al. 2001) were not considered because their lower statistics would not significantly improve the quality of the lightcurves.

The *XMM–Newton* EPIC-pn raw data have been processed using the EPCHAIN tool of SAS to obtain calibrated and concatenated event lists. The extraction radii and the optimal time cuts to exclude periods of high flaring particle background were computed via an iterative process which maximizes the signal-to-noise ratio (SNR), as described in Piconcelli et al. (2004), filtering out those time

[1] www.bass-survey.com

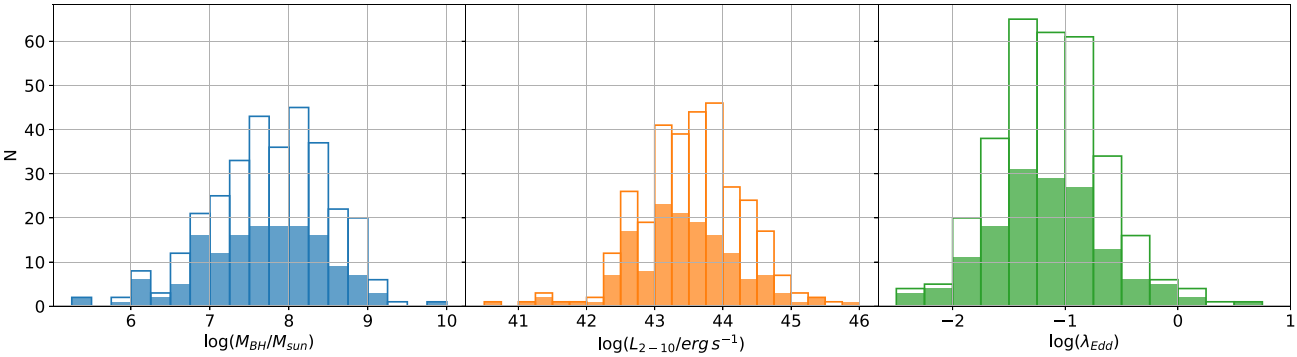

Figure 1. Distributions of black hole masses ($M_{\rm BH}$; left panel), 2–10 keV luminosities ($L_{2–10}$; middle panel), Eddington ratios ($\lambda_{\rm Edd}$; right panel) of the sources analysed in this work, compared with the parent BASS sample of unobscured AGNs (empty bars).

intervals for which the count rate of the background reach values so high that the SNR of the source does not improve (or even worsens) when including such time intervals in the analysis. Since the pn camera has a full-frame time resolution of 73.3 ms per CCD, the observations generally do not suffer significantly from pileup, making them suitable for variability analysis. Nonetheless, the light curves were extracted after confirming that the data were not affected by pileup, as indicated by the SAS task EPATPLOT. The resulting optimal extraction radius was ∼30–40 arcsec and the background spectra were extracted from source-free circular regions with radii of ∼50–60 arcsec for all the observations analysed in this work. With these regions we extracted the EPIC-pn source and background light curves using the command EVSELECT and we corrected the source light curve for the background using the command EPICLCCORR. We extracted the light curves using several different time and spectral binning strategies: 100 and 1000 s in the 0.2–10 keV energy band, and 100 s in the 0.2–1 (soft), 1–3 (medium), and 3–10 keV (hard) energy bands.

Following Ponti et al. (2012), we selected the observations which had cleaned exposure times larger than 10 ks, and which had at least 10 counts in those 10 ks chunks and in each (rest-frame) energy band used in this analysis, i.e. 0.2–1, 1–3, and 3–10 keV and for each time bin of 100 s and 1000 s. We did this selection to avoid having not enough counts in the 10 ks independent light curve to constrain the $\sigma^2_{\rm NXS}$. A total of 151 sources (∼500 observations) fulfil these criteria. The distributions of $M_{\rm BH}$, $L_{2–10}$, $\lambda_{\rm Edd}$, and $N_{\rm H}$ of our sample is shown in Fig. 1.

We show in Appendix A the *XMM–Newton* EPIC-pn background subctracted light curves of a sub-sample of representative sources for different $M_{\rm BH}$ values (see Fig. A1).

3 ANALYSIS

The excess variance ($\sigma^2_{\rm NXS}$) is a quantity used to describe the variability amplitude. It is the difference between the total variance of a light curve and the mean squared error that is normalized for the average of the N flux measurements squared (e.g. Nandra et al. 1997; Turner et al. 1999). Here N is the number of good time intervals in a light curve, and x_i and σ_i are the flux and error in each interval, respectively. The excess variance is defined (Vaughan et al. 2003) as follows:

$$\sigma^2_{\rm NXS} = \frac{S^2 - \overline{\sigma^2}}{\overline{x_i^2}}. \quad (1)$$

Where $\overline{\sigma^2}$ is the mean square error:

$$\overline{\sigma^2} = \frac{1}{N}\sum_{i=1}^{N}[\sigma_i^2], \quad (2)$$

and S^2 is the sample variance:

$$S^2 = \frac{1}{N-1}\sum_{i=1}^{N}[(x_i - \overline{x_i})^2], \quad (3)$$

corresponding to the integral of the PSD between two frequencies (ν_1 and ν_2), which yields the contribution to the expectation value of the variance due to variations between the corresponding time-scales ($1/\nu_1$ and $1/\nu_2$):

$$\langle S^2 \rangle = \int_{\nu_1}^{\nu_2} P(\nu)\mathrm{d}\nu. \quad (4)$$

To study the correlations between $\sigma^2_{\rm NXS}$ and $M_{\rm BH}$, $L_{2–10}$ and $\lambda_{\rm Edd}$, we calculated $\sigma^2_{\rm NXS}$ from the *XMM–Newton* light curves. The values are listed in Table 2.

$\sigma^2_{\rm NXS}$ is a good estimator of the intrinsic variance of a source but it has some biases. It is related to the integral of the PSD between two frequencies and thus depends on the length of the monitoring time interval, on the red-noise character of the X-ray variability and also, due to the effect of cosmological time dilation, on the redshift (Lawrence & Papadakis 1993; Green, McHardy & Lehto 1993; Lawrence & Papadakis 1993; Papadakis et al. 2008; Vagnetti, Turriziani & Trevese 2011; Vagnetti et al. 2016). Since our sample of 151 type 1 AGNs is composed mainly of local AGNs ($z_{\rm med} = 0.035$), the impact of redshift is negligible. However, we need to avoid biases related to the different exposure times of our observations and the red-noise character of the light curves. Therefore, we computed the $\sigma^2_{\rm NXS}$ from 10 ks-long independent light curve sections and, for the sources with cleaned exposure time that lasted for a multiple of 10 ks, we took the median of the excess variances of all these independent sections in each energy band. For the sources with more than one observation, we used the median value of the $\sigma^2_{\rm NXS}$ in both the cases of the light curves with 100 and 1000 s time bin in each energy band. We applied this procedure also for the seven sources of our sample which are classified as 'changing-look' AGNs (i.e. Mrk 1018, Fairall 9, Mrk 590, NGC 3516, NGC 1566, 3C 390.3, NGC 7603; Jin, Wu & Feng 2022; Temple et al. 2023) since the $\sigma^2_{\rm NXS}$ computed for these sources are consistent within the error among the different observations.

The X-ray spectrum of AGNs in different energy bands is strongly impacted by different components: the primary power-law

Table 1. Summary of the *XMM–Newton* observations of the sources (OBSID) of our sample together with the *Swift* identification name (*Swift* ID) and the *Swift* identification number (ID). This table is available in its entirety in a machine-readable form in the online journal. A part is shown as guidance for the reader regarding its content.

ID	*Swift*ID	OBSID
6	SWIFTJ0006.2+2012	0101040701
6	SWIFTJ0006.2+2012	0510010701
...		
16	SWIFTJ0029.2+1319	0783270201
34	SWIFTJ0051.6+2928	0903040301
36	SWIFTJ0051.9+1724	0801890301
39	SWIFTJ0054.9+2524	0301450401
39	SWIFTJ0054.9+2524	0841480101
43	SWIFTJ0059.4+3150	0312190101
61	SWIFTJ0113.8-1450	0147920101
73	SWIFTJ0123.9-5846	0101040201
73	SWIFTJ0123.9-5846	0721110201
...		
77	SWIFTJ0127.5+1910	0112600601
77	SWIFTJ0127.5+1910	0830551001
...		
106	SWIFTJ0206.2-0019	0201090201
106	SWIFTJ0206.2-0019	0554920301
...		

component and the reflection component are dominant in the hard energy band (3–10 keV; Haardt & Maraschi 1991, 1993; Haardt & Matt 1993) while soft-excess and warm-absorbers (WA) can impact the soft (0.2–1 keV; Bianchi et al. 2009) and medium (1–3 keV; Blustin et al. 2005; Tombesi et al. 2013) energy bands. Variations of these different components will lead to distinct spectral variability in different energy bands. We, therefore, calculated $\sigma^2_{\rm NXS}$ from the 0.2–1 (soft), 1–3 (medium), and 3–10 keV (hard) light curves to get a fuller picture of the AGNs X-ray variability.

3.1 Correlations between the normalized excess variance and the physical parameters

To investigate the physical parameters driving X-ray variability in our sample of unobscured AGNs, we looked for correlations between the *XMM–Newton* broad-band (0.2–10 keV) $\sigma^2_{\rm NXS}$ and several key AGNs parameters (i.e. $M_{\rm BH}$, L_{2-10}, $\lambda_{\rm Edd}$) by fitting a linear model to the data in the log–log space (see Figs 2 and 3) using the following fitting relation:

$$\log(\sigma^2_{\rm NXS}) = {\rm A} + {\rm B}\log({\rm x}), \quad (5)$$

where x is the value of the physical parameter. Among the 151 sources of our sample, we found 46 objects with an intrinsic $\sigma^2_{\rm NXS}$ lower than the respective error. In this case, we define the measurement as a 'non-detection', and we consider it as an upper limit. To include the upper limits in our analysis, we used the SA method (e.g. Feigelson & Nelson 1985; Shimizu et al. 2017) using the SCIKIT-SURVIVAL (Pölsterl 2020) package, which applies the principles of SA to astronomical data. SA is a statistical technique used to analyse time-to-event data and it is particularly well-suited for analysing data that include upper/lower limits. Specifically, SCIKIT-SURVIVAL calculates the non-parametric Kaplan-Meier product-limit (KMPL) estimator for a sample distribution. The KMPL estimator is an estimate of the survival function, which is simply 1-CDF (cumulative distribution function). Using the KMPL, we calculated for each bin of $M_{\rm BH}$, L_{2-10}, and $\lambda_{\rm Edd}$, the median $\sigma^2_{\rm NXS}$ and estimated their uncertainties. Since the KMPL estimator is a non-parametric method, it is unbiased because it does not assume any specific distribution for the data. We divided $M_{\rm BH}$ and $\lambda_{\rm Edd}$ into six bins and the L_{2-10} into seven bins. These bins are not symmetrical, since we requested each bin to have at least 15 values. We fitted the median values obtained with the SA method using the code: LINMIX, a hierarchical Bayesian model for fitting a straight line to data with errors in both the x and y directions (Kelly 2007). From the analysis of the correlation between $\sigma^2_{\rm NXS}$ and $M_{\rm BH}$, data of sources with $M_{\rm BH} > 10^9\,{\rm M}_\odot$ are excluded since, for these sources, we found mostly upper limits on $\sigma^2_{\rm NXS}$. So, being the last bin populated just by upper limits, the SA method was not reliable in computing the median in the bin.

We report in Table 3 the intercepts and the slopes of the linear regression line together with Pearson's correlation coefficients and the correlation probabilities for all the relations analysed in this work and for light curves with 100 and 1000 s bins. As shown in Table 3, the fitting parameters for the 100 and 1000 s binned light curves are consistent within the errors in each analysed relation.

Fig. 2 shows the $\sigma^2_{\rm NXS}$ versus $M_{\rm BH}$ relation obtained from the 0.2–10 keV light curves binned with 100 and 1000 s. We also reported the SA results for each bin. Being the SA results the $\sigma^2_{\rm NXS}$ median calculated using the KMPL estimator they are representative of the $\sigma^2_{\rm NXS}$ value in each $M_{\rm BH}$ bin. We also report the linear regressions obtained from the fitting over the SA results. As expected from previous studies (Nandra et al. 1997; Papadakis 2004; O'Neill et al. 2005; Ponti et al. 2012), we found a strong anticorrelation between $\sigma^2_{\rm NXS}$ and $M_{\rm BH}$ (see Fig. 2). We computed the 1σ scatter of the data around the best-fitting line using the following equation:

$$\sigma_{\rm scatter} = \sqrt{\sum_{i=1}^{N}[\log(\sigma^2_{\rm NXS,i}) - f(M_{\rm BH,i})]^2/N}, \quad (6)$$

where $f(M_{\rm BH})$ is the logarithmic value of the $\sigma^2_{\rm NXS}$ extrapolated using the best-fitting relation (see Table 3). We found a scatter for this relation of $\sim$0.85 dex in both the case of the light curves binned with 100 and 1000 s.

We also found a strong anticorrelation between the $\sigma^2_{\rm NXS}$ and the L_{2-10} (see upper panels of Fig. 3). Given the strong dependence between the $\sigma^2_{\rm NXS}$ and $M_{\rm BH}$, we decided to correct the $\sigma^2_{\rm NXS}$ for $M_{\rm BH}$ to check if after the correction, the relation between $\sigma^2_{\rm NXS}$ and L_{2-10} is still present. Previous works have shown that $\sigma^2_{\rm NXS} \propto M_{\rm BH}{}^{\sim(-1)}$ (e.g. Ponti et al. 2012). In this work, we found a slope for the $\sigma^2_{\rm NXS}$ versus $M_{\rm BH}$ relation of -0.77 ± 0.23 and -1.12 ± 0.18 when considering light curves with 100 and 1000 s bins, respectively. Since -1 is still consistent within the errors with our results, for consistency with past works, to check if the $\sigma^2_{\rm NXS}$ versus L_{2-10} correlation still exists when the primary dependence is removed, we analysed the correlation between $\sigma^2_{\rm NXS} \times M_{\rm BH}$ versus L_{2-10}. Removing the dependence of $\sigma^2_{\rm NXS}$ on $M_{\rm BH}$, the strong correlation with L_{2-10}, that was present before, is not significant anymore (see Fig. 4), as reported from previous studies (Papadakis 2004; O'Neill et al. 2005). In fact, we found in both cases of $\sigma^2_{\rm NXS}$ obtained from the 0.2–10 keV light curves binned with 100 and 1000 s, a Pearson correlation coefficient of -0.19 and -0.20 corresponding to a $1 - P_{\rm value}$ of 0.30 (see Table 3). Thus, the dependence between the $\sigma^2_{\rm NXS}$ and $L_{2-10\,{\rm keV}}$ is actually related to the dependence between $L_{2-10\,{\rm keV}}$ and $M_{\rm BH}$. From our analysis an anticorrelation between $\sigma^2_{\rm NXS}$ and $\lambda_{\rm Edd}$ is present (see lower panels of Fig. 3), but it is not significant, according to the Pearson test (see Table 3).

Table 2. List of the *Swift* ID, the *Swift* name (*Swift*ID), the counterpart name, the redshift (z), the hydrogen column density [$N_{\rm H}$ (cm^{-2})], the mass ($M_{\rm BH}$ in solar masses), the 2–10 keV luminosity [L_{2-10} (erg s^{-1})], the bolometric lumunosity [$L_{\rm bol}$ (erg s^{-1})], the Eddington ratio ($\lambda_{\rm Edd}$), the normalized excess variance for the light curves binned with 100 s ($\sigma^2_{\rm NXS,100\,s}$) and 1000s ($\sigma^2_{\rm NXS,1000\,s}$) of time binning. This table is available in its entirety in a machine-readable form in the online journal, where also the errors are reported. A part is shown as guidance for the reader regarding its content.

ID	*Swift*ID	Counterpart	z	log($N_{\rm H}$) (cm^{-2})	log($M_{\rm BH}$) ($M_{\rm sun}$)	log(L_{2-10}) (erg s^{-1})	log($L_{\rm bol}$) (erg s^{-1})	$\lambda_{\rm Edd}$	log($\sigma^2_{\rm NXS,100\,s}$)	log($\sigma^2_{\rm NXS,1000\,s}$)
6	SWIFTJ0006.2 + 2012	Mrk 335	0.025	20.48	7.23	43.23	44.36	0.068	−2.30	−2.30
16	SWIFTJ0029.2 + 1319	PG 0026+129	0.142	20.01	8.48	44.39	45.72	0.104	−3.63	−3.03
34	SWIFTJ0051.6 + 2928	UGC 524	0.036	20.02	7.62	42.99	44.08	0.032	−3.20	−3.20
36	SWIFTJ0051.9 + 1724	Mrk 1148	0.064	20.3	7.75	44.12	45.31	0.234	−4.54	−5.14
39	SWIFTJ0054.9 + 2524	PG 0052+251	0.155	20.02	8.46	44.62	45.89	0.135	−3.36	−3.99
43	SWIFTJ0059.4 + 3150	Mrk 352	0.014	20.01	7.55	42.72	44.09	0.016	−3.00	−3.00
61	SWIFTJ0113.8-1450	Mrk 1152	0.052	20.01	8.32	43.47	45.16	0.037	−3.13	−4.43
73	SWIFTJ0123.9-5846	Fairall 9	0.047	20.02	8.29	44.13	45.29	0.058	−2.22	−2.30
77	SWIFTJ0127.5 + 1910	Mrk 359	0.017	20.61	6.04	42.66	43.83	0.339	−2.69	−2.69
106	SWIFTJ0206.2-0019	Mrk 1018	0.042	20.01	7.81	43.61	45.08	0.094	−3.61	−4.03
...										

Note. The values of the $M_{\rm BH}$ are estimated from RM or broad lines (Koss et al. 2022c; Mejía-Restrepo et al. 2022; Ricci et al. 2022). $\lambda_{\rm Edd}$ are computed using the bolometric luminosities calculated from the intrinsic 14–150 keV luminosities as shown in Ricci et al. (2017) with a bolometric correction of 8 (Koss et al. 2022a). $N_{\rm H}$ and L_{2-10} from Ricci et al. (2017).

Table 3. List of the best-fitting relations together with their p-values. The fits are performed in the log–log space using equation (5).

Relation	Δt (s)	Intercept (A)	Slope (B)	Pearson	1 − $P_{\rm value}$
$\sigma^2_{\rm NXS}$ versus $M_{\rm BH}$	100	2.99 ± 1.79	−0.77 ± 0.23	−0.94	0.99
$\sigma^2_{\rm NXS}$ versus $M_{\rm BH}$	1000	5.54 ± 2.11	−1.12 ± 0.18	−0.96	0.99
$\sigma^2_{\rm NXS}$ versus L_{2-10}	100	26.29 ± 25.29	−0.67 ± 0.08	−0.84	0.95
$\sigma^2_{\rm NXS}$ versus L_{2-10}	1000	29.84 ± 36.41	−0.76 ± 0.06	−0.85	0.96
$\sigma^2_{\rm NXS}$ versus $\lambda_{\rm Edd}$	100	−3.55 ± 2.27	−0.36 ± 0.61	−0.10	0.25
$\sigma^2_{\rm NXS}$ versus $\lambda_{\rm Edd}$	1000	−3.11 ± 3.19	−0.24 ± 0.59	−0.12	0.25
$\sigma^2_{\rm NXS}$ versus $M_{\rm BH,RM}$	100	2.94 ± 0.29	−0.75 ± 0.20	−0.66	0.75
$\sigma^2_{\rm NXS}$ versus $M_{\rm BH,RM}$	1000	2.91 ± 0.34	−0.76 ± 0.41	−0.67	0.79
$\sigma^2_{\rm NXS}$ versus $M_{\rm BH}$ (L_{2-10} <$L_{2-10,\rm med}$)	100	0.36 ± 0.51	−0.43 ± 0.06	−0.89	0.97
$\sigma^2_{\rm NXS}$ versus $M_{\rm BH}$ (L_{2-10} <$L_{2-10,\rm med}$)	1000	0.16 ± 0.38	−0.37 ± 0.04	−0.99	0.99
$\sigma^2_{\rm NXS}$ versus $M_{\rm BH}$ (L_{2-10} >$L_{2-10,\rm med}$)	100	−2.45 ± 0.48	−0.14 ± 0.16	−0.30	0.38
$\sigma^2_{\rm NXS}$ versus $M_{\rm BH}$ (L_{2-10} >$L_{2-10,\rm med}$)	1000	−1.71 ± 0.41	−0.16 ± 0.15	−0.35	0.41
$\sigma^2_{\rm NXS}$ versus $M_{\rm BH}$ ($\lambda_{\rm Edd}$ <$\lambda_{\rm Edd,med}$)	100	0.69 ± 0.76	−0.48 ± 0.09	−0.89	0.97
$\sigma^2_{\rm NXS}$ versus $M_{\rm BH}$ ($\lambda_{\rm Edd}$ <$\lambda_{\rm Edd,med}$)	1000	1.46 ± 1.32	−0.55 ± 0.16	−0.89	0.97
$\sigma^2_{\rm NXS}$ versus $M_{\rm BH}$ ($\lambda_{\rm Edd}$ >$\lambda_{\rm Edd,med}$)	100	0.16 ± 0.83	−0.42 ± 0.13	−0.89	0.97
$\sigma^2_{\rm NXS}$ versus $M_{\rm BH}$ ($\lambda_{\rm Edd}$ >$\lambda_{\rm Edd,med}$)	1000	2.35 ± 0.88	−0.71 ± 0.11	−0.89	0.97
$\sigma^2_{\rm NXS}$ × $M_{\rm BH}$ versus L_{2-10}	100	14.35 ± 9.75	−0.26 ± 0.27	−0.19	0.30
$\sigma^2_{\rm NXS}$ × $M_{\rm BH}$ versus L_{2-10}	1000	12.05 ± 7.78	−0.21 ± 0.22	−0.20	0.30
$\sigma^2_{\rm NXS,hard}$ versus $\sigma^2_{\rm NXS,soft}$	100	−0.62 ± 0.26	0.87 ± 0.10	0.71	0.99
$\sigma^2_{\rm NXS,hard}$ versus $\sigma^2_{\rm NXS,med}$	100	−0.47 ± 0.22	0.93 ± 0.08	0.79	0.99

From Fig. 3 it is clear that in both relations a gradient of $M_{\rm BH}$ is present. Thus, to check if the relation $\sigma^2_{\rm NXS}$–$M_{\rm BH}$ is somehow affected by L_{2-10} and/or $\lambda_{\rm Edd}$, we first computed the median values of L_{2-10} and $\lambda_{\rm Edd}$ of the sample, which are $L_{2-10,\rm med} = 2.79 \times 10^{43}$ erg s^{-1} and $\lambda_{\rm Edd,med} = 0.06$, respectively. We then used these values as thresholds to divide the sample into two sub-samples depending on their L_{2-10} and $\lambda_{\rm Edd}$ (see Fig. 5). The best-fitting values of the correlations we found are also reported in Table 3. We found that the correlation between $\sigma^2_{\rm NXS}$ and $M_{\rm BH}$ has slightly different normalizations among the two sub-samples depending on the L_{2-10} or $\lambda_{\rm Edd}$ but the same slope within the errors, which is also in agreement with the slope of the $\sigma^2_{\rm NXS}$–$M_{\rm BH}$ relation found for the total sample. In particular, in the sub-sample depending on L_{2-10} we found that the slopes of the correlations is similar to the one found for the total sample, while the normalization for the sources with $L_{2-10} > L_{2-10,\rm med}$ is lower. This is not really surprising since sources with high luminosity (high $M_{\rm BH}$) show lower variability. Also, the majority of the sources with $L_{2-10} > L_{2-10,\rm med}$ show an upper limit of the $\sigma^2_{\rm NXS}$.

3.2 Reverberation mapping sub-sample

We checked the relation between the $\sigma^2_{\rm NXS}$ and $M_{\rm BH}$ in the sub-sample of sources in which $M_{\rm BH}$ is obtained via RM (35 sources). Being the sub-sample smaller, we did not used the SA method. Instead we used the method of the 'censored fitting' (CF; Guainazzi et al. 2006; Bianchi et al. 2009), to account for upper limits. This was done by performing a large number of least-square fits, using the LINMIX code, on a set of Monte Carlo simulated data derived from the observed data points. Each detection was substituted by a value randomly drawn from a Gaussian distribution, whose mean is the best-fitting measurement and whose standard deviation is its

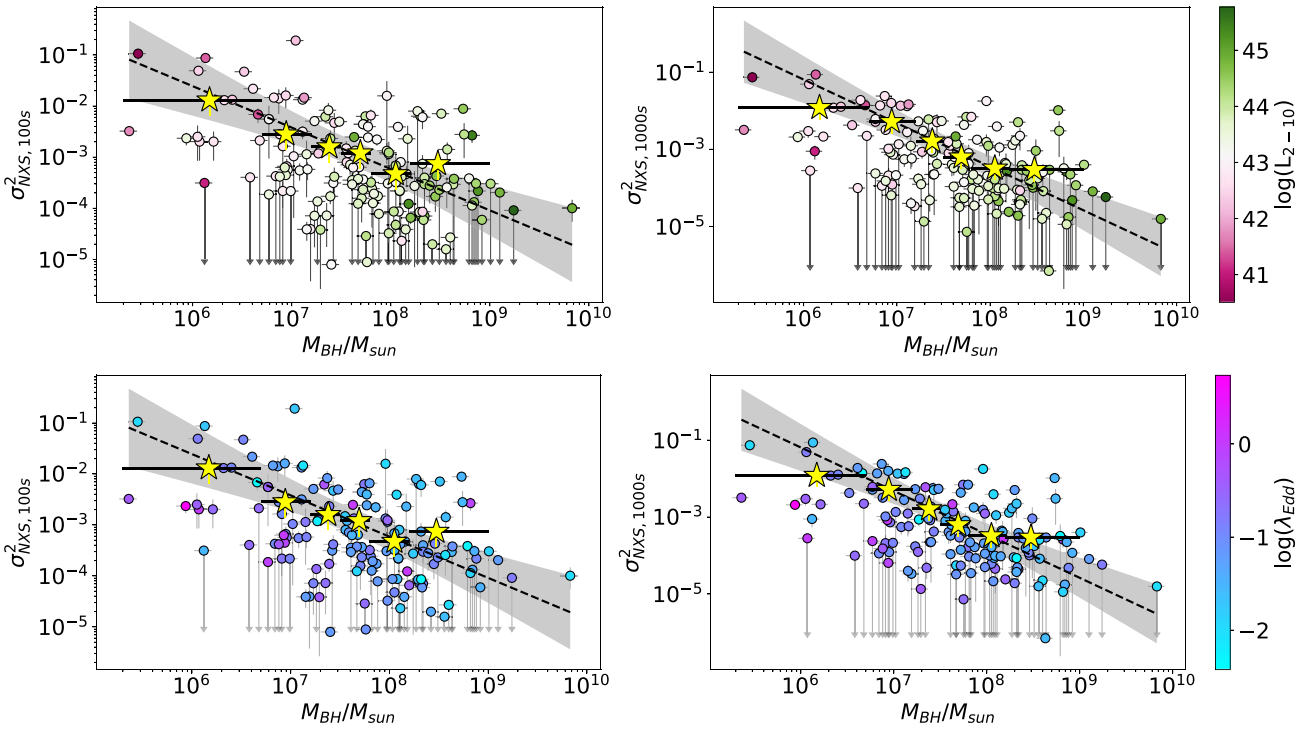

Figure 2. $\sigma^2_{\rm NXS}$ versus $M_{\rm BH}$ relation obtained from the 0.2–10 keV light curves binned with 100 s (left panels) and 1000 s (right panels). Yellow stars with error bars correspond to the survival analysis (SA) results for each bin. The dashed lines are the linear regressions obtained from the fitting over the SA results, while the shaded region represents the combined 1σ error on the slope and normalization. Each coloured data points with error bars represents one source of our sample. Colourbars represent the $L_{2–10}$ (top panels) and $\lambda_{\rm Edd}$ (bottom panels).

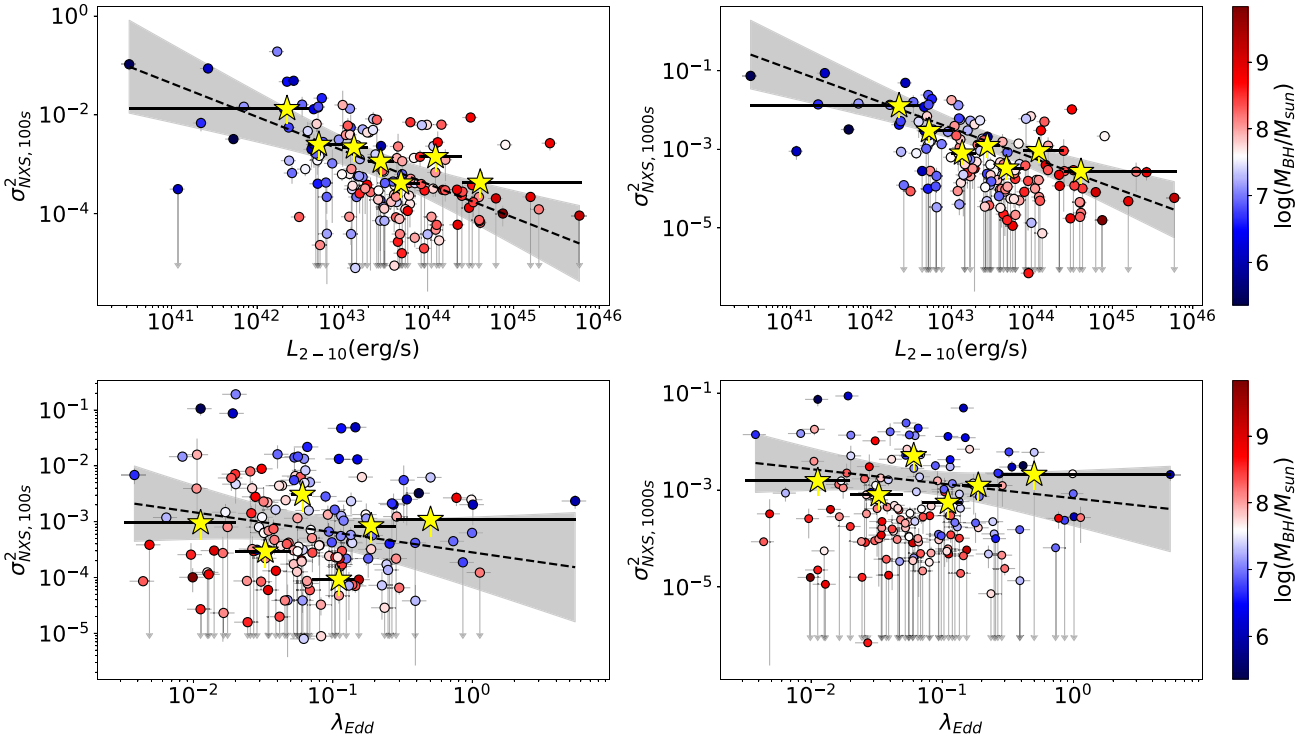

Figure 3. Upper panels: $L_{2–10}$ versus $M_{\rm BH}$ relation. Lower panels: $\lambda_{\rm Edd}$ versus $\sigma^2_{\rm NXS}$ relations. The relations are obtained from the 0.2–10 keV light curves binned with 100 (left panels) and 1000 s (right panels). Yellow stars with error bars correspond to the SA results for each bin. The dashed lines are the linear regressions obtained from the fitting over the SA results, while the shaded region represents the combined 1σ error on the slope and normalization. Each coloured data points with error bars represents one source of our sample. Colourbars represent the $M_{\rm BH}$.

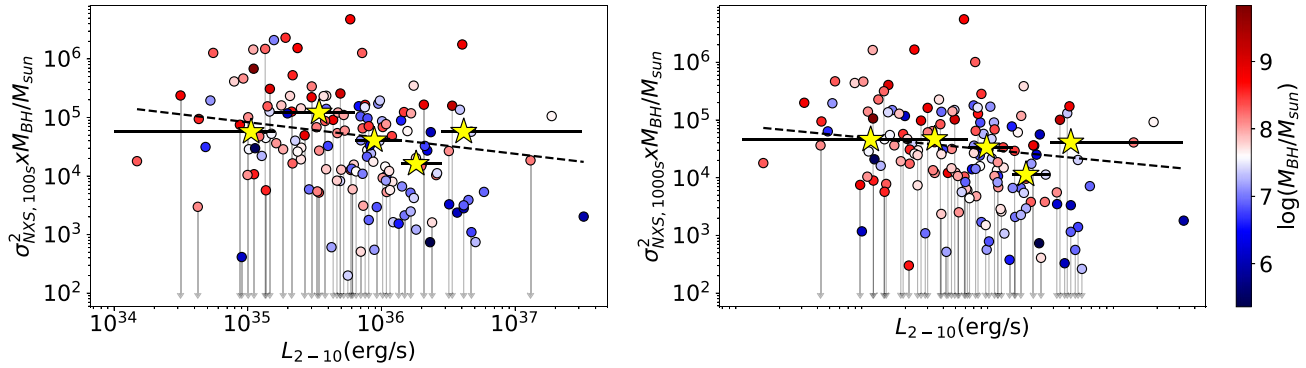

Figure 4. $\sigma^2_{\rm NXS} \times M_{\rm BH}$ versus $L_{2–10}$ relation. The relations are obtained from the 0.2–10 keV light curves binned with 100 (left panels) and 1000 s (right panels). Yellow stars with error bars correspond to the SA results for each bin. The dashed lines are the linear regressions obtained from the fitting over the SA results. Colourbars represent the $M_{\rm BH}$.

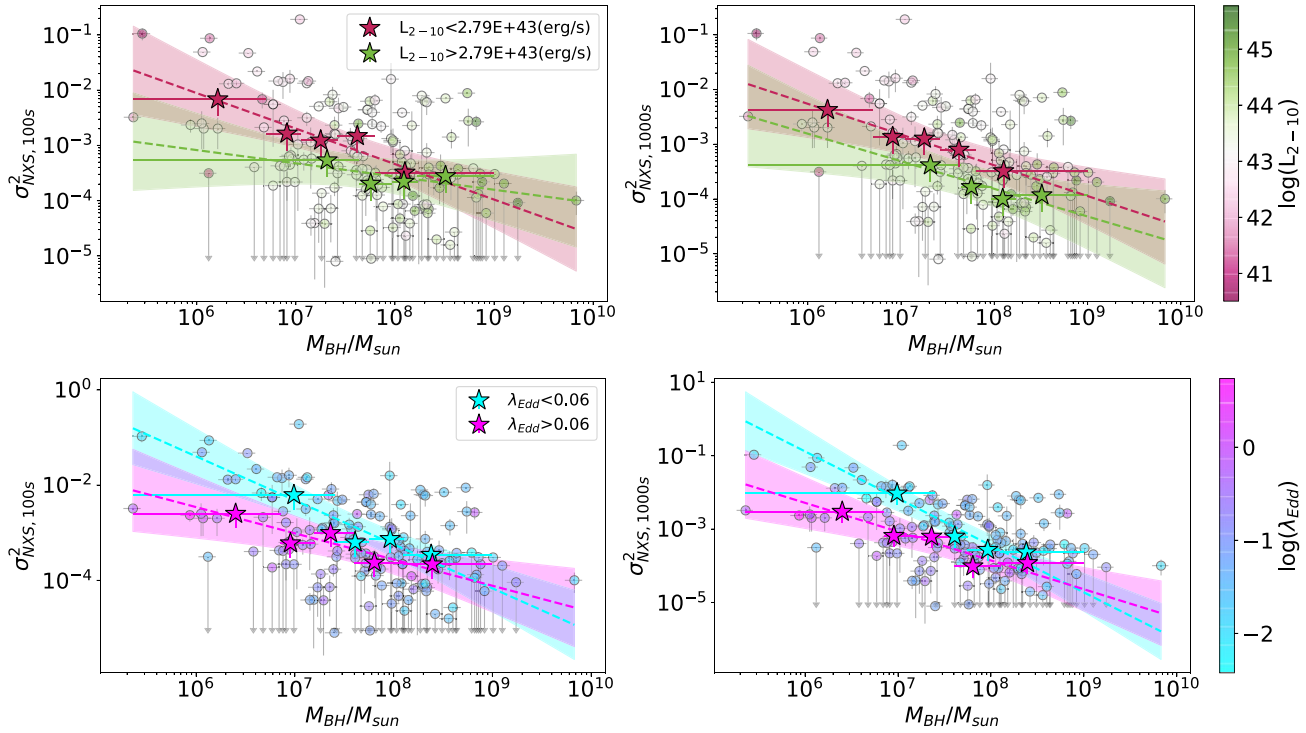

Figure 5. Relations between the $\sigma^2_{\rm NXS}$ versus $M_{\rm BH}$ when the sample is divided into two bins of $L_{2–10}$ (top panels; purple lines: $L_{2–10} < L_{2–10,\rm med}$, green lines: $L_{2–10} > L_{2–10,\rm med}$) and $\lambda_{\rm Edd}$ (bottom panels; cyan lines: $\lambda_{\rm Edd} < \lambda_{\rm Edd,med}$, magenta lines: $\lambda_{\rm Edd} > \lambda_{\rm Edd,med}$). The best-fitting relation are reported in Table 3.

statistical uncertainty. Each upper limit U was substituted by a value randomly drawn from a uniform distribution in the interval $[A, U]$, where A was arbitrarily set to $A \ll U$. We choose $A = 10^{-6}$. We found an anticorrelation in both cases of $\sigma^2_{\rm NXS}$ obtained from the 0.2–10 keV light curves binned with 100 and 1000 s (see Fig. 6). Using equation (6) we found $\sigma_{\rm scatter,100} = 0.65$ and 0.69, smaller than the scatters of the $\sigma^2_{\rm NXS}$ versus $M_{\rm BH}$ relations obtained from the total sample. This is because on average the sources with $M_{\rm BH}$ estimated via RM are brighter and they show a higher count rate on the same time-scales. Using the $\sigma^2_{\rm NXS}$ versus $M_{\rm BH}$ relations obtained from the RM sample, it is possible to measure $M_{\rm BH}$ for a total of 87 AGNs (out of 151 AGNs in our sample) and provide an upper/lower limit for the remaining AGN. Thus, even if the X-ray variability is not the most accurate tool to measure $M_{\rm BH}$, the relation obtained for the RM sub-sample gives a good $M_{\rm BH}$ estimation, with a scatter <1 dex.

3.3 The normalized excess variance in the soft, medium, and hard energy bands

It is interesting to compare $\sigma^2_{\rm NXS}$ in various energy bands to check if there is one or more components of the AGNs X-ray spectrum that contributes the most in the variability. In order to verify this, we calculated $\sigma^2_{\rm NXS}$ in the the soft (0.2–1 keV), medium (1–3 keV), and hard (3–10 keV) bands. We then looked for a correlation between the $\sigma^2_{\rm NXS,hard}$ and both $\sigma^2_{\rm NXS,soft}$ and $\sigma^2_{\rm NXS,med}$. In the left panel of Fig. 7, we show $\sigma^2_{\rm NXS}$ in the soft energy band versus the same parameter

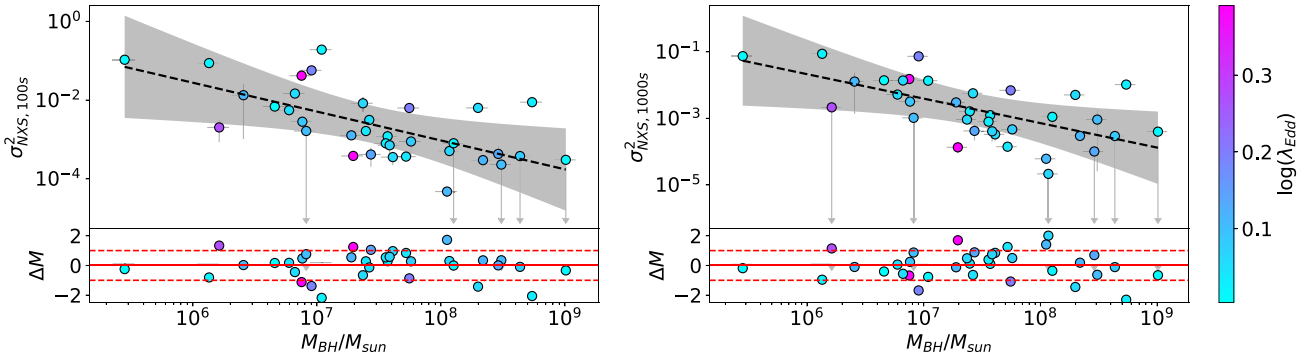

Figure 6. $\sigma^2_{\rm NXS}$ versus $M_{\rm BH}$ for the RM sub-sample. The dashed black lines are the linear regressions obtained from the fitting process. Shaded region represents the combined 1σ error on the slope and normalization. The $\sigma^2_{\rm NXS}$ is obtained from the 0.2–10 keV light curves binned with 100 (left panel) and 1000 s (right panels). Lower panels show the difference between the real $M_{\rm BH}$ and $M_{\rm BH}$ extrapolated from the relation (ΔM). For details about the coefficients, see Table 3.

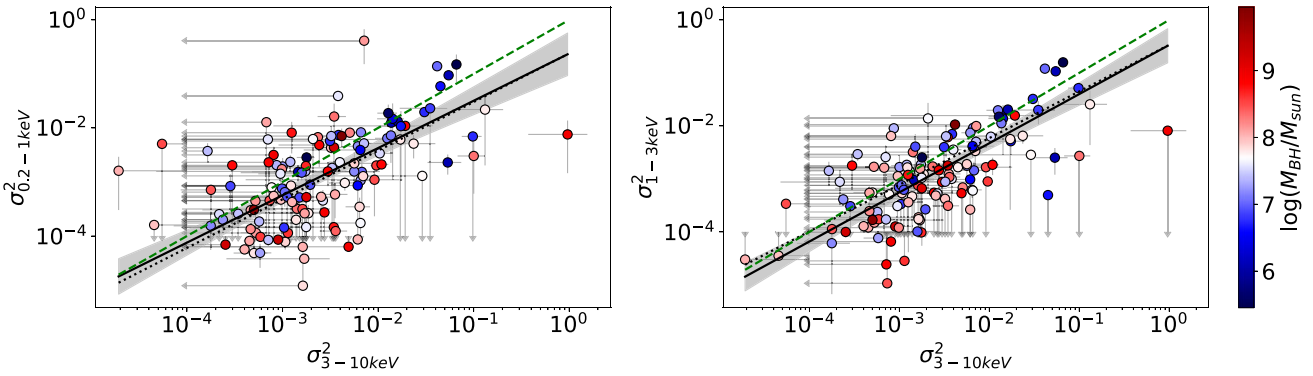

Figure 7. Left panel: soft (0.2–1 keV) versus hard (3–10 keV) $\sigma^2_{\rm NXS}$. Right panel: medium (1–3 keV) versus hard (3–10 keV) $\sigma^2_{\rm NXS}$. The best-fitting curves are plotted with solid black lines while the shaded region represents the combined 3σ error on the slope and intercept. The green dashed lines represent the one-to-one relation. Black dashed lines represent the regression lines found using the bisector method.

calculated in the hard band, while in the right panel of Fig. 7 we illustrate the excess variance in the medium energy band versus that in the hard band. The best-fitting relations, reported in Table 3, are obtained using the CF method (see Section 3.2).

We fitted the data also with the bisector method which provides a more balanced and symmetric estimate of the true regression line between the two variables that in principle could be independent. The values of the slope and intercept we found with this method are consistent within the errors with the one found using the CF method.

The values of $\sigma^2_{\rm NXS}$ in the soft and medium energy bands appear to be well correlated with $\sigma^2_{\rm NXS}$ in the hard energy band, although with a slope flatter than the one-to-one relation (green dashed line in Fig. 7). This may imply that for most of our sources, on time-scales less than 10 ks the spectral components which dominate in the hard band are increasingly more variable than the ones dominating the soft and medium energy bands, for higher values of the variance. In the soft energy band the dominant component is usually the soft-excess, which can be variable. Furthermore, in the soft-medium energy bands, the presence of absorbing material, either neutral or ionized, can be variable or can absorb the continuum emission responding to the continuum variations. If these variations happened on time-scales less than ∼10 ks, we would expect to measure a larger variability amplitude in the soft/medium energy bands compared to the hard band. We observe the opposite, i.e. weaker variations of the soft-excess and/or WA than those of the primary continuum and/or reflection component on this time-scale, in agreement with previous studies (Ponti et al. 2012; Simm et al. 2016).

For completeness, we checked the relations between the $\sigma^2_{\rm NXS}$ in the soft, medium, and hard energy bands with the physical properties of the AGN ($M_{\rm BH}$, L_{2-10}, and $\lambda_{\rm Edd}$) to see whether these relations support the results found in this work. The best-fitting results are reported in Appendix B. We found that the $\sigma^2_{\rm NXS}$ versus $M_{\rm BH}$ relation in the soft energy band is slightly less significant than in the harder energy bands (see Table B1), but in general the best-fitting relations in each energy band are consistent with those from the broad *XMM–Newton* energy band (0.2–10 keV).

4 CONCLUSIONS

We analysed the variability properties of ∼500 *XMM–Newton* observations of a sample of 151 nearby ($z_{\rm med} = 0.035$) unobscured ($N_{\rm H} < 10^{22}$ cm^{-2}) AGNs from the BASS survey, studying the correlations of the excess variance with the physical properties of the sources and also checking for the correlations between the excess variance computed in different energy bands. The time-scale used to compute the $\sigma^2_{\rm NXS}$ is 10 ks, to avoid biases related to the differences on the exposure times of the sources of our sample and to take into account the red-noise character of the light curves. We analysed the relations of $\sigma^2_{\rm NXS}$ with $M_{\rm BH}$, L_{2-10}, and $\lambda_{\rm Edd}$. The correlation between $\sigma^2_{\rm NXS}$ and $M_{\rm BH}$ is a well-known property of AGNs (Lu & Yu 2001; Papadakis 2004; O'Neill et al. 2005; Nikołajuk et al. 2006; Nikolajuk,

Gurynowicz & Czerny 2007; Miniutti et al. 2009; Zhou et al. 2010; Ponti et al. 2012). In agreement with this, in our sample we found a very strong and highly significant correlation between these two quantities.

We do not find a significant correlation between $\sigma^2_{\rm NXS}$ and $\lambda_{\rm Edd}$, consistently with previous results (O'Neill et al. 2005; Gierliński, Nikołajuk & Czerny 2008; Zhou et al. 2010; Ponti et al. 2012; Lanzuisi et al. 2014). However, according to McHardy et al. (2006) the break time-scale increases proportionally as $M_{\rm BH}$ decreases ($\lambda_{\rm Edd}$ increases). Thus, if we assume a universal PDS with a single break frequency depending on the $M_{\rm BH}$ and a equally long-timescale normalization, the strength of the relations $\sigma^2_{\rm NXS}$ versus $M_{\rm BH}$, and $\sigma^2_{\rm NXS}$ versus $\lambda_{\rm Edd}$ would be the same, with higher short-timescale variability for low $M_{\rm BH}$ (high $\lambda_{\rm Edd}$). Our result could suggest that there might be no correlation between break time-scale and $\lambda_{\rm Edd}$, as proposed by González-Martín & Vaughan (2012) analysing a larger sample of shorter light curves. Alternatively, following the results of McHardy et al. (2006) and Paolillo et al. (2017), $\lambda_{\rm Edd}$ could be dependent on the break time-scale but, since on short-timescale $\sigma^2_{\rm NXS}$ seems mostly independent of this parameter, the normalization of the power spectrum may be anticorrelated with $\lambda_{\rm Edd}$.

We found a tight anticorrelation between $\sigma^2_{\rm NXS}$ and L_{2-10}. To remove the $M_{\rm BH}$ dependence from this correlation, we explored the relation between the $\sigma^2_{\rm NXS} \times M_{\rm BH}$ versus L_{2-10}, finding that, in this case, the $\sigma^2_{\rm NXS}$ versus L_{2-10} correlation disappears, confirming that the correlation with L_{2-10} is secondary, while the primary correlation is in fact with the mass, in agreement with what has been found by previous works (e.g. Papadakis 2004; O'Neill et al. 2005; Lanzuisi et al. 2014).

We explored the $\sigma^2_{\rm NXS}$ versus $M_{\rm BH}$ relation in the sub-sample of sources with $M_{\rm BH}$ estimated via RM, finding that the correlation between these quantities in this sub-sample has an intrinsic scatter of ∼0.65–0.69 dex. With this relation we were able to measure $M_{\rm BH}$ for 87 AGNs and estimate upper/lower limits for the remaining 64 AGNs of our sample. Thus, one could in principle use X-ray variability to measure $M_{\rm BH}$ (e.g. Nikolajuk, Papadakis & Czerny 2004; Ponti et al. 2012; Akylas et al. 2022). With the advent of future planned or proposed missions (e.g. *Athena*, *AXIS*, etc) that will provide higher count rates, the accuracy of this relation for mass measurement will improve significantly.

Dividing the sample into two bins of L_{2-10}, the normalization of the anticorrelation between $\sigma^2_{\rm NXS}$ and $M_{\rm BH}$ is lower for the sources with higher luminosity. This is possibly related to the fact that for sources with high-luminosity (high mass), we detected lower variability and mostly only an upper limit on $\sigma^2_{\rm NXS}$ was obtained. When dividing the sample into two bins of $\lambda_{\rm Edd}$ the slope and the normalization are slightly different in the two sub-samples but still consistent within the errors.

X-ray spectra could be dominated by different components depending on the energy band one is analysing. Therefore, we explored the relation of the $\sigma^2_{\rm NXS}$ in the hard X-ray band (3–10 keV) with the $\sigma^2_{\rm NXS}$ in the soft X-ray band (0.2–1 keV) and in the medium X-ray band (1–3 keV), finding that $\sigma^2_{\rm NXS}$ calculated in various energy bands are highly correlated, in agreement with previous studies (Ponti et al. 2012; Simm et al. 2016). In particular, we found that in most sources the primary continuum and/or the reflection component are increasingly more variable than the spectral components dominating softer energy bands (0.2–1 keV and 1–3 keV) on time-scales shorter than 10 ks. In fact, if WA components were varying, they would show more variability in the medium energy band, while the variance in that band is lower than in the hard energy band. Thus WA variability cannot be generally the cause of fast (shorter than 10 ks) variations. Moreover, we found that the soft energy band is less variable than the hard band. This implies that the soft-excess, or at least part of it, is a less variable component (on time-scales less than 10 ks) which dilutes the $\sigma^2_{\rm NXS}$ by adding to the constant flux in the denominator and not to the variable flux in the numerator, as it was found for the Seyfert 1.5 galaxy NGC 3227 (Arévalo & Markowitz 2014). Finally, the hard continuum might be intrinsically more variable than the continuum in softer bands because the break time-scale of the PDS moves to shorter time-scales for higher energy X-ray photons (McHardy et al. 2004; McHardy et al. 2007; Markowitz et al. 2007; Arévalo, McHardy & Summons 2008).

We examined the relation between $\sigma^2_{\rm NXS}$ (calculated in the soft, medium, and hard X-ray bands) and several important AGN physical parameters, such as $M_{\rm BH}$, L_{2-10}, and $\lambda_{\rm Edd}$. Our analysis revealed that the best-fitting relations in each energy band align with those from the broad *XMM–Newton* energy band (0.2–10 keV). Notably, in the soft energy band, the $\sigma^2_{\rm NXS}$ versus $M_{\rm BH}$ anticorrelation appears to be slightly less significant. This lends support to another key finding of this study, i.e. that, on time-scales shorter than 10 ks, the primary continuum and/or the reflection component exhibit stronger variability compared to the spectral components dominating softer energy bands.

Compared with previous results (e.g. Ponti et al. 2012), we found a less steep correlation between $\sigma^2_{\rm NXS}$ and $M_{\rm BH}$. The difference could be attributed to the larger number of black hole masses from reverberation mapping, to the higher quality optical measurements and fitting for the other mass measurements techniques, and also to the larger number of observations used (a factor ∼2 larger than Ponti et al. 2012), which helped to refine the computation of $\sigma^2_{\rm NXS}$. Our results are consistent with the common picture in which, as a general rule, nearby AGNs display similar patterns of variability once they are rescaled for $M_{\rm BH}$ and $\lambda_{\rm Edd}$.

ACKNOWLEDGEMENTS

This work was funded by ANID programs FONDECYT Postdoctorado – 3190213 (AT), 3220516 (MT), 3210157 (ARL); FONDECYT Regular – 1230345 (CR) and 1200495 (FEB); Millennium Science Initiative Programme – ICN12_009 (FEB); CATA-BASAL – ACE210002 (FEB) and FB210003 (CR, FEB). TL acknowledges support from the NANOGrav NSF Physics Frontiers Center No. 2020265. BT acknowledges support from the European Research Council (ERC) under the European Union's Horizon 2020 research and innovation program (grant agreement number 950533) and from the Israel Science Foundation (grant number 1849/19). TK is supported by JSPS KAKENHI grant no. 23K13153 and acknowledges support by the Special Postdoctoral Researchers Program at RIKEN. KO acknowledges support from the National Research Foundation of Korea (NRF-2020R1C1C1005462) and the Korea Astronomy and Space Science Institute under the R&D program (Project No. 2023-1-868-03) supervised by the Ministry of Science and ICT. This work is based on observations obtained with the ESA science mission *XMM–Newton*, with instruments and contributions directly funded by ESA Member States and the USA (NASA). The authors thank the anonymous referee for constructive comments that have helped in improving the quality of the paper.

DATA AVAILABILITY

All the data utilized in this paper are publicly available in the *XMM–Newton* data archive at https://nxsa.esac.esa.int/nxsa-web/#search. More details of the observations are listed in Table 1.

REFERENCES

Akylas A., Papadakis I., Georgakakis A., 2022, A&A, 666, A127
Arévalo P., Markowitz A., 2014, ApJ, 783, 82
Arévalo P., McHardy I. M., Summons D. P., 2008, MNRAS, 388, 211
Barr P., Mushotzky R. F., 1986, Nature, 320, 421
Barthelmy S. D. et al., 2005, Space Sci. Rev., 120, 143
Bian W., Zhao Y., 2002, A&A, 395, 465
Bian W., Zhao Y., 2003, MNRAS, 343, 164
Bianchi S., Guainazzi M., Matt G., Fonseca Bonilla N., Ponti G., 2009, A&A, 495, 421
Blustin A. J., Page M. J., Fuerst S. V., Branduardi-Raymont G., Ashton C. E., 2005, A&A, 431, 111
Cackett E. M., Bentz M. C., Kara E., 2021, iScience, 24, 102557
De Marco B., Motta S. E., Belloni T. M., 2022, in Cosimo B. Andrea S., eds, Handbook of X-ray and Gamma-ray Astrophysics. Springer, Berlin
den Herder J. W. et al., 2001, A&A, 365, L7
Feigelson E. D., Nelson P. I., 1985, ApJ, 293, 192
Gabriel C. et al., 2004, in Ochsenbein F., Allen M. G., Egret D., eds, ASP Conf. Ser. Vol. 314, Astronomical Data Analysis Software and Systems (ADASS) XIII. Astron. Soc. Pac, San Francisco, p. 759
Gehrels N. et al., 2004, ApJ, 611, 1005
Gierliński M., Nikołajuk M., Czerny B., 2008, MNRAS, 383, 741
González-Martín O., Vaughan S., 2012, A&A, 544, A80
Green A. R., McHardy I. M., Lehto H. J., 1993, MNRAS, 265, 664
Guainazzi M., Siemiginowska A., Stanghellini C., Grandi P., Piconcelli E., Azubike Ugwoke C., 2006, A&A, 446, 87
Haardt F., Maraschi L., 1991, ApJ, 380, L51
Haardt F., Maraschi L., 1993, ApJ, 413, 507
Haardt F., Matt G., 1993, MNRAS, 261, 346
Ichikawa K., Ricci C., Ueda Y., Matsuoka K., Toba Y., Kawamuro T., Trakhtenbrot B., Koss M. J., 2017, ApJ, 835, 74
Ichikawa K. et al., 2019, ApJ, 870, 31
Ishibashi W., Courvoisier T. J. L., 2009, A&A, 504, 61
Jansen F. et al., 2001, A&A, 365, L1
Jin J.-J., Wu X.-B., Feng X.-T., 2022, ApJ, 926, 184
Kawamuro T. et al., 2022, ApJ, 938, 87
Kelly B. C., 2007, ApJ, 665, 1489
Koss M. et al., 2017, ApJ, 850, 74
Koss M. J. et al., 2018, Nature, 563, 214
Koss M. J. et al., 2021, ApJS, 252, 29
Koss M. J. et al., 2022a, ApJS, 261, 1
Koss M. J. et al., 2022b, ApJS, 261, 2
Koss M. J. et al., 2022c, ApJS, 261, 6
Lamperti I. et al., 2017, MNRAS, 467, 540
Lanzuisi G. et al., 2014, ApJ, 781, 105
Lawrence A., Papadakis I., 1993, ApJ, 414, L85
Lawrence A. et al., 2016, MNRAS, 463, 296
Lu Y., Yu Q., 2001, MNRAS, 324, 653
Ludlam R. M., Cackett E. M., Gültekin K., Fabian A. C., Gallo L., Miniutti G., 2015, MNRAS, 447, 2112
McHardy I. M., 2001, in Peterson B. M., Pogge R. W., Polidan R. S., eds, ASP Conf. Ser. Vol. 224, Probing the Physics of Active Galactic Nuclei. Astron. Soc. Pac. , San Francisco, p. 205
McHardy I. M., Papadakis I. E., Uttley P., Page M. J., Mason K. O., 2004, MNRAS, 348, 783
McHardy I. M., Koerding E., Knigge C., Uttley P., Fender R. P., 2006, Nature, 444, 730
McHardy I. M., Arévalo P., Uttley P., Papadakis I. E., Summons D. P., Brinkmann W., Page M. J., 2007, MNRAS, 382, 985
Markowitz A., Edelson R., Vaughan S., 2003, ApJ, 598, 935
Markowitz A., Papadakis I., Arévalo P., Turner T. J., Miller L., Reeves J. N., 2007, ApJ, 656, 116
Masterson M. et al., 2022, ApJ, 934, 35
Mejía-Restrepo J. E. et al., 2022, ApJS, 261, 5
Miniutti G., Ponti G., Greene J. E., Ho L. C., Fabian A. C., Iwasawa K., 2009, MNRAS, 394, 443
Mushotzky R. F., Done C., Pounds K. A., 1993, ARA&A, 31, 717
Nandra K., George I. M., Mushotzky R. F., Turner T. J., Yaqoob T., 1997, ApJ, 476, 70
Nikolajuk M., Papadakis I. E., Czerny B., 2004, MNRAS, 350, L26
Nikołajuk M., Czerny B., Ziółkowski J., Gierliński M., 2006, MNRAS, 370, 1534
Nikolajuk M., Gurynowicz P., Czerny B., 2007, in Ho L. C., Wang J. W., eds, ASP Conf. Ser. Vol. 373, The Central Engine of Active Galactic Nuclei. Astron. Soc. Pac., San Francisco, p. 66
O'Neill P. M., Nandra K., Papadakis I. E., Turner T. J., 2005, MNRAS, 358, 1405
Oh K. et al., 2018, ApJS, 235, 4
Oh K. et al., 2022, ApJS, 261, 4
Paolillo M. et al., 2017, MNRAS, 471, 4398
Papadakis I. E., 2004, MNRAS, 348, 207
Papadakis I. E., McHardy I. M., 1995, MNRAS, 273, 923
Papadakis I. E., Chatzopoulos E., Athanasiadis D., Markowitz A., Georgantopoulos I., 2008, A&A, 487, 475
Phillipson R. A., Vogeley M. S., Boyd P. T., 2023, MNRAS, 518, 4372
Piconcelli E., Jimenez-Bailón E., Guainazzi M., Schartel N., Rodríguez-Pascual P. M., Santos-Lleó M., 2004, MNRAS, 351, 161
Pölsterl S., 2020, J. Mach. Learn. Res., 21, 1
Ponti G., Papadakis I., Bianchi S., Guainazzi M., Matt G., Uttley P., Bonilla N. F., 2012, A&A, 542, A83
Ricci C., Trakhtenbrot B., 2022, preprint (arXiv:2211.05132)
Ricci C., Ueda Y., Koss M. J., Trakhtenbrot B., Bauer F. E., Gandhi P., 2015, ApJ, 815, L13
Ricci C. et al., 2017, ApJS, 233, 17
Ricci C. et al., 2020, ApJ, 898, L1
Ricci C. et al., 2021, ApJS, 255, 7
Ricci F. et al., 2022, ApJS, 261, 8
Ricci C. et al., 2023, ApJ, 952, L28
Rumbaugh N. et al., 2018, ApJ, 854, 160
Salpeter E. E., 1964, ApJ, 140, 796
Sartori L. F., Schawinski K., Trakhtenbrot B., Caplar N., Treister E., Koss M. J., Megan Urry C., Zhang C., 2018, MNRAS, 476, L34
Shen Y., 2021, ApJ, 921, 70
Shimizu T. T., Mushotzky R. F., 2013, ApJ, 770, 60
Shimizu T. T., Mushotzky R. F., Meléndez M., Koss M. J., Barger A. J., Cowie L. L., 2017, MNRAS, 466, 3161
Simm T., Salvato M., Saglia R., Ponti G., Lanzuisi G., Trakhtenbrot B., Nandra K., Bender R., 2016, A&A, 585, A129
Soldi S. et al., 2014, A&A, 563, A57
Strüder L. et al., 2001, A&A, 365, L18
Temple M. J. et al., 2023, MNRAS, 518, 2938
Timlin John D. I., Brandt W. N., Zhu S., Liu H., Luo B., Ni Q., 2020, MNRAS, 498, 4033
Tombesi F., Cappi M., Reeves J. N., Nemmen R. S., Braito V., Gaspari M., Reynolds C. S., 2013, MNRAS, 430, 1102
Trakhtenbrot B. et al., 2019, ApJ, 883, 94
Turner T. J., George I. M., Nandra K., Turcan D., 1999, ApJ, 524, 667
Turner M. J. L. et al., 2001, A&A, 365, L27
Ulrich M.-H., Maraschi L., Urry C. M., 1997, ARA&A, 35, 445
Uttley P., McHardy I. M., 2005, MNRAS, 363, 586
Uttley P., McHardy I. M., Papadakis I. E., 2002, MNRAS, 332, 231
Uttley P., Cackett E. M., Fabian A. C., Kara E., Wilkins D. R., 2014, A&A Rev., 22, 72
Vagnetti F., Turriziani S., Trevese D., 2011, A&A, 536, A84
Vagnetti F., Middei R. Antonucci M., Paolillo M. Serafinelli R., 2016, A&A, 593, A55
Vaughan S., Edelson R., Warwick R. S., Uttley P., 2003, MNRAS, 345, 1271
Zeltyn G. et al., 2022, ApJ, 939, L16
Zhou X.-L., Zhang S.-N., Wang D.-X., Zhu L., 2010, ApJ, 710, 16

SUPPORTING INFORMATION

Supplementary data are available at *MNRAS* online.

Table 1. Summary of the *XMM–Newton* observations of the sources (OBSID) of our sample together with the *Swift* identification name (*Swift* ID) and the *Swift* ID.

Table 2. List of the *Swift* ID, the *Swift* name (*Swift*ID), the counterpart name, the redshift (z), the hydrogen column density [N_H (cm^{-2})], the mass (M_{BH} in solar masses), the 2–10 keV luminosity [L_{2-10} (erg s^{-1})], the bolometric lumunosity [L_{bol} (erg s^{-1})], the Eddington ratio (λ_{Edd}), the normalized excess variance for the light curves binned with 100s ($\sigma^2_{NXS\ 100s}$) and 1000s ($\sigma^2_{NXS\ 1000s}$)of time binning.

Please note: Oxford University Press is not responsible for the content or functionality of any supporting materials supplied by the authors. Any queries (other than missing material) should be directed to the corresponding author for the article.

APPENDIX A: LIGHT CURVES

We show in Fig. A the *XMM–Newton* EPIC-pn light curves (background subtracted) in the 0.2–10 keV energy band and with a time binning of 100 s for some representative sources of the sample:

(i) NGC 4593, $\log(M_{BH}/M_\odot) = 4.45$;
(ii) Mrk 359, $\log(M_{BH}/M_\odot) = 6.05$;
(iii) NGC 4748, $\log(M_{BH}/M_\odot) = 6.40$;
(iv) NGC 4593, $\log(M_{BH}/M_\odot) = 6.88$;
(v) Fairall 51, $\log(M_{BH}/M_\odot) = 7.12$;
(vi) Mrk 817, $\log(M_{BH}/M_\odot) = 7.59$;
(vii) Mrk 1018, $\log(M_{BH}/M_\odot) = 7.81$;
(viii) Ark 120, $\log(M_{BH}/M_\odot) = 8.07$;
(ix) 3C111 $\log(M_{BH}/M_\odot) = 8.45$;
(x) PG 1545+210, $\log(M_{BH}/M_\odot) = 8.84$;
(xi) PKS 2135−147, $\log(M_{BH}/M_\odot) = 9.10$;
(xii) 4C74p26, $\log(M_{BH}/M_\odot) = 9.83$.

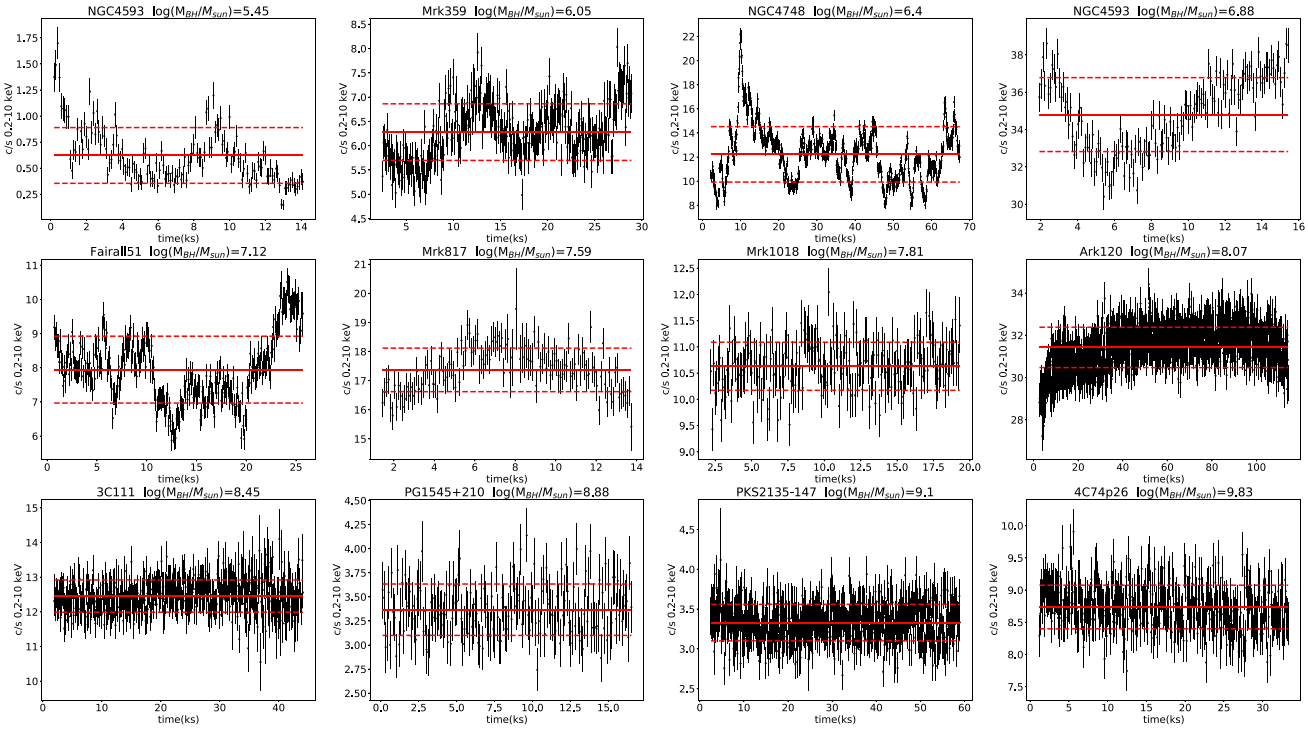

Figure A1. *XMM–Newton* EPIC-pn light curves (background subtracted) in the 0.2–10 keV with a time binning of 100 s are shown for some representative sources of the sample. From the top to the bottom and from the left to the right we reported the light curves for: NGC 4593, Mrk 359, NGC 4748, NGC 4593, Fairall 51, Mrk 817, Mrk 1018, Ark 120, 3C 111, PG 1545+210, PKS 2135−147, and 4C74+26. The red solid and dashed lines indicate the average and the standard error of the mean, respectively.

Table B1. List of the best-fitting relations together with their p-values for the $\sigma^2_{\rm NXS}$ in the soft, medium, and hard energy bands. The fits are performed in the log–log space using equation equation (5).

Relation	Intercept (A)	Slope (B)	Pearson	$1 - P_{\rm value}$
$\sigma^2_{\rm NXS,soft}$ versus $M_{\rm BH}$	1.23 ± 1.08	-0.68 ± 0.16	-0.61	0.79
$\sigma^2_{\rm NXS,med}$ versus $M_{\rm BH}$	2.58 ± 1.45	-0.73 ± 0.25	-0.87	0.98
$\sigma^2_{\rm NXS,hard}$ versus $M_{\rm BH}$	2.67 ± 1.32	-0.79 ± 0.28	-0.89	0.98
$\sigma^2_{\rm NXS,soft}$ versus L_{2-10}	16.65 ± 5.06	-0.44 ± 0.11	-0.85	0.98
$\sigma^2_{\rm NXS,med}$ versus L_{2-10}	12.06 ± 6.00	-0.34 ± 0.14	-0.71	0.92
$\sigma^2_{\rm NXS,hard}$ versus L_{2-10}	18.06 ± 5.64	-0.47 ± 0.13	-0.83	0.99
$\sigma^2_{\rm NXS,soft}$ versus $\lambda_{\rm Edd}$	-3.31 ± 0.25	-0.67 ± 0.20	-0.34	0.57
$\sigma^2_{\rm NXS,med}$ versus $\lambda_{\rm Edd}$	-2.93 ± 0.24	-0.29 ± 0.19	-0.29	0.33
$\sigma^2_{\rm NXS,hard}$ versus $\lambda_{\rm Edd}$	-2.77 ± 0.23	-0.44 ± 0.19	-0.15	0.29

APPENDIX B: RELATIONS BETWEEN THE EXCESS VARIANCE IN THE SOFT, MEDIUM, AND HARD ENERGY BAND AND THE AGN PHYSICAL QUANTITIES

We checked the relations between $\sigma^2_{\rm NXS}$ in the soft (0.2–1 keV), medium (1–3 keV), and hard (3–10 keV) energy bands with $M_{\rm BH}$, L_{2-10}, and $\lambda_{\rm Edd}$ to see whether these relations support the results found in this work or not. For the analysis, we applied the same method described in Section 3. The best-fitting results are shown in Tab. B1. For both $\sigma^2_{\rm NXS}$ versus $M_{\rm BH}$ and $\sigma^2_{\rm NXS}$ versus L_{2-10}, the relations we found in the different energy bands are consistent with the ones in the total *XMM–Newton* energy band (0.2–10 keV). It is worthwhile to underline that, in the case of the $\sigma^2_{\rm NXS}$ versus $M_{\rm BH}$ relation, the anticorrelation is slightly less significant in the soft energy band. This can be related to the other result of this paper according to which the primary continuum and/or of the reflection component (the spectral component dominating the hard energy band) are increasingly more variable than the spectral components dominating other energy bands on time-scales shorter than 10 ks. In the case of the $\sigma^2_{\rm NXS}$ versus $\lambda_{\rm Edd}$, we found an anticorrelation which is still not statistically significant that became less stronger in the medium and hard energy bands.

[1]*Instituto de Estudios Astrofísicos, Facultad de Ingeniería y Ciencias, Universidad Diego Portales, Av. Ejército Libertador 441, Santiago 8320000, Chile*
[2]*INAF Osservatorio Astronomico di Roma, Via Frascati 33, Monte Porzio Catone 00078 (RM), Italy*
[3]*Kavli Institute for Astronomy and Astrophysics, Peking University, Beijing 100871, China*
[4]*Department of Physics & Astronomy, George Mason University, MS 3F3, 4400 University Drive, Fairfax, VA 22030, USA*
[5]*Instituto de Física y Astronomía, Facultad de Ciencias, Universidad de Valparaíso, Gran Bretana N 1111, Playa Ancha, Valparaíso 2390418, Chile*
[6]*Eureka Scientific, 2452 Delmer Street Suite 100, Oakland, CA 94602-3017, USA*
[7]*Instituto de Astrofísica, Facultad de Física, Pontificia Universidad Católica de Chile, Campus San Joaquín, Av. Vicuña Mackenna 4860, Santiago 7820436, Chile*
[8]*Centro de Astroingeniería, Facultad de Física, Pontificia Universidad Católica de Chile, Campus San Joaquín, Av. Vicuña Mackenna 4860, Santiago 7820436, Chile*
[9]*Millennium Institute of Astrophysics, Nuncio Monseñor Sótero Sanz 100, Of 104, Providencia, Santiago, Chile*
[10]*Space Science Institute, 4750 Walnut Street, Suite 205, Boulder, Colorado 80301, USA*
[11]*School of Physics and Astronomy, Tel Aviv University, Tel Aviv 69978, Israel*
[12]*Department of Astronomy, University of Maryland, College Park, MD 20742, USA*
[13]*Joint Space-Science Institute, University of Maryland, College Park, MD 20742, USA*
[14]*Dipartimento di Matematica e Fisica, Università degli Studi Roma Tre, via della Vasca Navale 84, I-00146 Roma, Italy*
[15]*Centro de Astronomía (CITEVA), Universidad de Antofagasta, Avenida Angamos 601, Antofagasta 1240000, Chile*
[16]*RIKEN Cluster for Pioneering Research, 2-1 Hirosawa, Wako, Saitama 351-0198, Japan*
[17]*Department of Physics, Southern Methodist University, 3215 Daniel Ave., Dallas, TX 75205, USA*
[18]*Department of Physics and Astronomy, West Virginia University, P.O. Box 6315, Morgantown, WV 26506, USA*
[19]*Cahill Center for Astronomy and Astrophysics, California Institute of Technology, Pasadena, CA 91125, USA*
[20]*Korea Astronomy & Space Science institute, 776, Daedeokdae-ro, Yuseong-gu, Daejeon 34055, Republic of Korea*
[21]*Department of Astronomy, Kyoto University, Kitashirakawa-Oiwake-cho, Sakyo-ku, Kyoto 606-8502, Japan*
[22]*Kavli Institute for Particle Astrophysics and Cosmology, Stanford University, 452 Lomita Mall, Stanford, CA 94305, USA*
[23]*Jet Propulsion Laboratory, California Institute of Technology, 4800 Oak Grove Drive, MS 169-224, Pasadena, CA 91109, USA*
[24]*Yale Center for Astronomy & Astrophysics and Department of Physics, Yale University, PO Box 208120, New Haven, CT 06520-8120, USA*

This paper has been typeset from a TEX/LATEX file prepared by the author.